

Possible Multi-band Afterglows of FRB 20171020A and its Implication

KE BIAN¹ AND CAN-MIN DENG¹¹Guangxi Key Laboratory for Relativistic Astrophysics, Department of Physics, Guangxi University, Nanning 530004, China; dengcm@gxu.edu.cn

ABSTRACT

Fast Radio Bursts (FRBs) are millisecond-duration radio transients of mysterious origin, with growing evidence linking at least some of them to magnetars. While FRBs are primarily observed in the radio band, their potential multi-wavelength afterglows remain largely unexplored. We investigate the possible afterglow of FRB 20171020A, a rare nearby and bright FRB localized in a galaxy at only 37 Mpc. Assuming that this source produces a future bright burst, we model the expected afterglow emission in the radio, optical, and X-ray bands under both uniform and wind-like ambient media, within the framework of the magnetar model. Our results show that the optical afterglow is the most promising for detection, but it fades rapidly and requires follow-up within a few hundred seconds post-burst. The radio afterglow may be detectable under favorable conditions in a dense stellar wind, whereas the X-ray counterpart is too faint for current telescopes. These findings suggest that rapid optical follow-up offers the best opportunity to detect the afterglow of the next bright burst from FRB 20171020A, providing unique insights into the progenitor and its environment. To assess observational feasibility, we estimate the event rate of nearby FRBs with sufficient energy to power detectable afterglows, finding a rate of ~ 0.3 per year for CHIME surveys. Although this rate is low and the optical detection timescale is short, coordinated fast-response strategies using global telescope networks could significantly improve the chance of success. As more nearby FRBs are discovered, multi-wavelength observations will be essential in unveiling the physical nature of these enigmatic events.

1. INTRODUCTION

Fast Radio Bursts (FRBs) are millisecond-duration radio transients of extragalactic origin, exhibiting extreme luminosities and diverse observational properties. Since their discovery (Lorimer et al. 2007; Thornton et al. 2013), extensive efforts have been made to understand their progenitors and emission mechanisms (Xiao et al. 2021; Zhang 2023; Lorimer et al. 2024). While magnetars have emerged as a leading candidate for at least some FRBs, as evidenced by the association of FRB 200428D with the Galactic magnetar SGR 1935+2154 (CHIME/FRB Collaboration et al. 2020; Bochenek et al. 2020; Lin et al. 2020), the observed diversity in FRB properties—including repetition rates, polarization variability, and host galaxy environments—suggests multiple progenitor channels or environmental influences (CHIME/FRB Collaboration et al. 2019; Kumar et al. 2019; Li et al. 2021; Kirsten et al. 2022; CHIME/FRB Collaboration et al. 2021; Pleunis et al. 2021; Nimmo et al. 2021; Feng et al. 2022; Xu et al. 2022; Chime/Frb Collaboration et al. 2023).

Recent large-sample surveys, such as those conducted by CHIME/FRB, have greatly expanded our knowledge of FRBs, revealing a wide range of behaviors and host

galaxy types. Some FRBs are found in dwarf star-forming galaxies, while others are located in globular clusters or older stellar populations. This diversity suggests that the FRB population likely consists of multiple progenitor classes (Zhang 2023). Proposed progenitor models span magnetar flares, neutron star mergers, accretion-induced collapses, white dwarf interactions, and even exotic scenarios such as primordial black hole evaporation (Platts et al. 2020; Zhang 2020). A growing number of FRBs are found to repeat, while others show only a single detected burst, further complicating the picture.

One of the promising approaches to unraveling the nature of FRBs is the search for their multi-wavelength afterglows (Yi et al. 2014; Nicastro et al. 2021). Similar to gamma-ray bursts, FRB explosions may eject relativistic material, which interacts with the surrounding medium to produce afterglow emission across the electromagnetic spectrum (Metzger et al. 2019; Beloborodov 2020; Margalit et al. 2020). The detectability and evolution of such afterglows depend strongly on the energy of the ejected material and the properties of the circum-burst environment. Recent studies have shown that afterglow observations could help distinguish between dif-

ferent FRB models. For instance, [Cooper et al. \(2022\)](#) examined the lack of a detected afterglow from FRB 200428D and argued that a simple, constant-density environment was unlikely, while a wind-like medium could better explain the observations. [Du et al. \(2023\)](#) also conducted an analysis of the multi-band afterglow of FRB 200428D using the standard external shock synchrotron emission model commonly applied to gamma-ray bursts.

Despite growing theoretical interest, afterglow detections remain elusive, likely due to the short duration and low energy output of typical FRBs, as well as the often large distances involved. Detectability may be improved for nearby and unusually bright FRBs, which provide a rare opportunity to probe the surrounding medium and the nature of the outflows. In this context, nearby FRBs with high fluence are of particular observational interest.

Here, we focus on FRB 20171020A, an exceptional FRB discovered by ASKAP ([Sokolowski et al. 2018](#)) and localized in its host galaxy, ESO 601-G036, at a distance of just 37 Mpc ([Mahony et al. 2018; Lee-Waddell et al. 2023](#)). This makes it one of the closest extragalactic FRBs. What makes FRB 20171020A even more remarkable is its extraordinary brightness of 200 Jy ms, ranking it among the brightest FRBs localized by ASKAP so far ([Arcus et al. 2025](#)). Its unique combination of proximity and high brightness makes it a prime candidate for afterglow studies, presenting a rare opportunity to probe the circum-burst environment and relativistic ejecta energetics, given its high fluence suggesting a substantial energy reservoir for detectable afterglows.

In this work, we conduct a theoretical investigation into the potential multi-wavelength afterglow of FRB 20171020A. By modeling the dynamics of the FRB ejecta and its interaction with different external environments—specifically, a uniform interstellar medium and a stellar wind—we derive the expected light curves in the radio, optical, and X-ray bands and compare them with the sensitivity limits of current and upcoming observational facilities. It is important to emphasize that no afterglow was detected following the previous burst of FRB 20171020A due to the lack of timely follow-up observations. Therefore, our predictions pertain to the afterglow that might accompany its next burst in the future. Given the source’s relatively close distance and high fluence, FRB 20171020A stands as an excellent candidate for targeted follow-up observations. This study not only deepens our understanding of FRB 20171020A but also provides a framework for optimizing follow-up strategies for nearby, bright FRBs, which in turn can help constrain FRB progenitor models and the characteristics of their surrounding environments.

2. MODEL DESCRIPTION

To investigate the possible multi-wavelength afterglow of FRB 20171020A, we adopt the flaring magnetar model, in which a relativistic outflow from a magnetar collides with the surrounding medium, producing synchrotron maser emission at the shock front ([Metzger et al. 2019; Margalit et al. 2020](#)). This process not only generates the prompt FRB emission, but also deposits energy into the external medium, potentially leading to a long-lived afterglow. Following this framework, we model the interaction between the FRB ejecta and its environment, and calculate the resulting afterglow light curves in the radio, optical, and X-ray bands.

2.1. Dynamics of the Ejecta

Following the production of FRB emission, the relativistic ejecta continues to propagate outward, sweeping up ambient material and producing synchrotron afterglow emission. We consider this relativistic ejecta with an initial kinetic energy E_k and an initial Lorentz factor η . As the ejecta propagates into the surrounding medium, it undergoes deceleration due to the accumulation of swept-up material. In order to unify the description of the early and late dynamical evolution of the blast wave, we adopt the formula given by [Huang et al. \(1999\)](#)

$$\frac{d\Gamma}{dM_s} = -\frac{\Gamma^2 - 1}{M_{ej} + \epsilon M_s + 2(1 - \epsilon)\Gamma M_s}, \quad (1)$$

where Γ is the Lorentz factor of the blast wave, and ϵ is the fraction of the shock-generated thermal energy that is radiated. M_s represents the mass inside a given radius r , which is defined by

$$M_s = \int_0^r m_p n(r) 4\pi r^2 dr', \quad (2)$$

where the number density $n(r)$ of the surrounding medium scaling as $n(r) \propto r^{-k}$. $k = 0$ represents the uniform medium, and $k = 2$ represents the wind-like medium. One can derive the relationship between Γ and r by substituting M_s into Equation (1). Moreover, using the relation of $r = ct/(1 - \beta)$, one can derive the relationship between Γ and time t of the observer, where β is the velocity of the shocked material, and $\Gamma = (1 - \beta^2)^{-1/2}$.

2.2. Thermal Synchrotron Emission

As the ejecta decelerate, a forward shock forms. In the parameter space considered in this work, the lifetime of the reverse shock is very short, in the order of ms. Given this short duration, we focus solely on the afterglow

emission produced by the forward shock., accelerating electrons and amplifying magnetic fields. These relativistic electrons then produce synchrotron radiation across multiple wavelengths, resulting in a broadband afterglow. In the standard afterglow models of gamma-ray bursts, relativistic shocks are often assumed to accelerate electrons into a non-thermal power-law distribution via the diffusive shock acceleration process. However, in the case considered in this work, the external medium surrounding FRBs is expected to be highly magnetized ($\sigma \gtrsim 0.1$) (Metzger et al. 2019; Margalit et al. 2020). In such an environment, the strong magnetic field suppresses particle diffusion across the shock front, leading to the breakdown of the standard Fermi acceleration mechanism (Sironi & Spitkovsky 2009). As a result, instead of a non-thermal power-law distribution, the electrons in the shocked region are expected to follow a thermal distribution characterized by

$$\gamma_s = \frac{m_p}{2m_e} \Gamma, \quad (3)$$

where m_p and m_e are the proton and electron masses, respectively. In a magnetized shock, the downstream magnetic field B is amplified due to compression and can be estimated as

$$B = \sqrt{32\pi\sigma\Gamma^2 n m_p c^2}, \quad (4)$$

where σ represents the magnetization of the upstream medium. We adopted $\sigma = 10^{-1}$ in this work following (Cooper et al. 2022), as required for coherent maser emission for FRBs (Metzger et al. 2019).

For synchrotron radiation of an electron with Lorentz factor γ_e , the observed radiation power and the characteristic frequency are given by

$$P(\gamma_e) \simeq \frac{4}{3} \sigma_T c \Gamma^2 \gamma_e^2 \frac{B^2}{8\pi}, \quad (5)$$

and

$$\nu(\gamma_e) \simeq \Gamma \gamma_e^2 \frac{q_e B}{2\pi m_e c}, \quad (6)$$

where q_e is the electron charge.

For an individual electron, the spectral power P_ν (in $\text{erg Hz}^{-1} \text{s}^{-1}$) varies as $\nu^{1/3}$ for $\nu < \nu(\gamma_e)$, and cuts off exponentially for $\nu > \nu(\gamma_e)$ (Blandford & McKee 1976). The peak power occurs at $\nu(\gamma_e)$, with an approximate value of

$$P_{\nu,\text{max}} \approx \frac{P(\gamma_e)}{\nu(\gamma_e)} = \frac{m_e c^2 \sigma_T}{3q_e} \Gamma B. \quad (7)$$

The synchrotron radiation spectrum is characterized by a multi-segment broken power law with an exponential cutoff at higher frequencies, with key frequencies:

the critical synchrotron frequency ν_s , the cooling frequency ν_c , and the self-absorption frequency ν_a .

The cooling frequency is given by

$$\nu_c = \frac{q_e B}{m_e c} \Gamma \gamma_c^2. \quad (8)$$

The critical synchrotron frequency of the shocked electrons is

$$\nu_s = \frac{q_e B}{2\pi m_e c} \Gamma \gamma_s^2. \quad (9)$$

The self-absorption frequency is given by

$$\nu_a = \begin{cases} \left[\frac{c_1(p-1)}{3-k} \frac{q_e n R}{B \gamma_s^5} \right]^{3/5} \nu_s, & \text{if } \nu_a < \nu_s, \\ \left[\frac{c_2(p-1)}{3-k} \frac{q_e n R}{B \gamma_s^5} \right]^{2/(p+5)} \nu_s, & \text{if } \nu_s < \nu_a < \nu_c. \end{cases} \quad (10)$$

where c_1, c_2 are coefficients that depend on p (Wu et al. 2003).

The luminosity observed by the observer is given by

$$L_{\nu,\text{max}} = N_e P_{\nu,\text{max}}, \quad (11)$$

where $N_e = M_s/m_p$ is the total number of electrons participating in the radiation.

Since the electrons remain thermalized rather than forming a power-law tail, their synchrotron emission is expected to differ significantly from conventional afterglow models, with a spectrum more closely resembling thermal synchrotron radiation rather than the usual broken power-law shape. In the context of this study, the electrons undergo fast cooling during the early stage, which switches to slow cooling at the later stage. The timescale at which this transition occurs is on the order of tens of seconds. At early times, the electrons are in the fast-cooling regime ($\nu_c < \nu_s$), where the spectral flux is given by (Sari et al. 1998; Gao et al. 2013)

$$L_\nu = \begin{cases} (\nu/\nu_a)^2 (\nu_a/\nu_c)^{1/3} L_{\nu,\text{max}}, & \nu < \nu_a \\ (\nu/\nu_c)^{1/3} L_{\nu,\text{max}}, & \nu_a < \nu < \nu_s \\ (\nu/\nu_c)^{-1/2} L_{\nu,\text{max}}, & \nu_c < \nu < \nu_s \\ \exp(1 - (\nu/\nu_s)) (\nu/\nu_s)^{1/2} L_{\nu,\text{max}}, & \nu_s < \nu, \end{cases} \quad (12)$$

for (a) $\nu_a < \nu_c < \nu_s$, and

$$L_\nu = \begin{cases} (\nu/\nu_c)^2 (\nu_c/\nu_a)^3 L_{\nu,\text{max}}, & \nu < \nu_c \\ (\nu/\nu_a)^{5/2} (\nu_a/\nu_c)^{-1/2} L_{\nu,\text{max}}, & \nu_c < \nu < \nu_s \\ (\nu/\nu_c)^{-1/2} L_{\nu,\text{max}}, & \nu_a < \nu < \nu_s \\ \exp(1 - (\nu/\nu_s)) (\nu/\nu_s)^{1/2} L_{\nu,\text{max}}, & \nu_s < \nu, \end{cases} \quad (13)$$

for (b) $\nu_c < \nu_a < \nu_s$. At later times, as the ejecta expand and cool, the electrons transition to the slow-cooling regime, where

$$L_\nu = \begin{cases} (\nu/\nu_a)^2 (\nu_a/\nu_s)^{1/3} L_{\nu,\text{max}}, & \nu < \nu_a \\ (\nu/\nu_s)^{1/3} L_{\nu,\text{max}}, & \nu_a < \nu < \nu_s \\ \exp(1 - (\nu/\nu_s)) (\nu/\nu_s)^{1/2} L_{\nu,\text{max}}, & \nu_s < \nu, \end{cases} \quad (14)$$

for (a) $\nu_a < \nu_s < \nu_c$, and

$$L_\nu = \begin{cases} (\nu/\nu_{\text{syn}})^2 (\nu_{\text{syn}}/\nu_a)^{(p+4)/2} L_{\nu,\text{max}}, & \nu < \nu_s \\ \exp(1 - (\nu/\nu_s)) (\nu/\nu_s)^{1/2} L_{\nu,\text{max}}, & \nu_s < \nu, \end{cases} \quad (15)$$

for (b) $\nu_s < \nu_a < \nu_c$. This spectral framework provides a robust description of thermal synchrotron emission from the forward shock, capturing its temporal and spectral evolution under various radiative regimes.

3. RESULTS

We present the theoretical multi-wavelength afterglow light curves of FRB 20171020A, considering two different external environments: a uniform medium (ISM) and a wind-like medium. Our calculations are based on the thermal synchrotron radiation model described in Section 2, and the results are displayed in Figure ?? (uniform case) and Figure 2 (wind case). For each scenario, we compute light curves in the radio (1 GHz), optical (R-band), and X-ray (1 keV) bands, and compare them with the detection limits of Very Large Array (VLA), which scales as $\propto t^{-1/2}$ for arbitrarily long exposure times. In survey mode, Legacy Survey of Space and Time (LSST) at the Vera C. Rubin Observatory reaches 24.5 mag in 30 s (Yi et al. 2014), and the X-ray telescope (XRT) onboard the Neil Gehrels Swift Observatory is $\propto t^{-1}$ early on and breaks to $\propto t^{-1/2}$ when $F_v = 2.0 \times 10^{-15} \text{ erg cm}^{-2} \text{ s}^{-1}$ at $t = 10^5 \text{ s}$ (Moretti et al. 2008). We also consider both radiative ($\epsilon = 1$) and adiabatic ($\epsilon = 0$) cases, where ϵ represents the efficiency of radiative losses of the blast wave. The kinetics of adiabatic evolution ($\epsilon = 0$) correspond to an optimistic scenario, whereas the kinetics of radiative evolution ($\epsilon = 1$) reflect a conservative situation.

3.1. Model Parameters and Justification

To compute the afterglow evolution of FRB 20171020A, we adopt key physical parameters based on theoretical models and observational constraints. The chosen values for the kinetic energy of the ejecta (E_k), initial Lorentz factor (η), and external medium density (n_0 for a uniform medium, M_w for a wind environment) are consistent with the magnetar model proposed by Metzger et al. (2019). Below, we detail the rationale behind each parameter selection.

The total kinetic energy of the relativistic ejecta is taken as $E_k = 10^{43} \text{ erg}$. This choice is motivated by comparisons with the Galactic FRB 200428D, which was associated with the magnetar SGR 1935+2154. The radiation efficiency of FRB 200428D was estimated to be 10^{-5} (Margalit et al. 2020), implying that the total energy released in the event is approximately 10^5 times the observed FRB energy. Given that FRB 20171020A

has an observed isotropic energy of 10^{38} erg (Sokolowski et al. 2018), we scale up the kinetic energy using the same efficiency factor, yielding $E_k = 10^{43} \text{ erg}$. This is consistent with theoretical expectations for magnetar-powered relativistic outflows (Metzger et al. 2019).

The initial Lorentz factor η governs the initial velocity of the ejecta and plays a crucial role in determining the afterglow evolution. We adopt different values for the uniform and wind medium scenarios. $\eta = 400$ for the uniform medium case, and $\eta = 15$ for the wind medium case. These values are directly taken from the magnetar model of Metzger et al. (2019).

The density of the surrounding medium affects how quickly the ejecta decelerate and determines the peak time and flux of the afterglow. For a uniform medium, we take the number density n in the range of $1\text{--}10^4 \text{ cm}^{-3}$ following Cooper et al. (2022). This value is consistent with the conditions required for coherent maser emission in FRBs, as derived in Metzger et al. (2019). For a stellar wind environment, the density profile follows

$$n(r) = \frac{\dot{M}_w}{4\pi r^2 v_w m_p},$$

where \dot{M}_w is the mass-loss rate, and v_w is the speed of the wind. We adopt \dot{M}_w in the value range of $10^{15}\text{--}10^{19} \text{ g s}^{-1}$, and $v_w = 0.5c$ (Metzger et al. 2019; Cooper et al. 2022). This is the characteristic mass-loss rate required in Metzger et al. (2019) for magnetar-driven outflows interacting with a surrounding wind.

These values ensure that our modeling remains consistent with FRB emission models while providing a robust framework for evaluating the detectability of FRB 20171020A's afterglow. With these parameters established, the following sections show how they influence the radio, optical, and X-ray afterglows, and how different environments impact the detectability of FRB 20171020A. It is worth clarifying that the afterglow emissions discussed in this work refer to potential afterglows associated with future bursts from the source FRB 20171020A, rather than any afterglow following its previously detected burst. In other words, our results provide predictions for the detectability of multi-wavelength afterglows assuming FRB 20171020A emits a new, bright burst in the future. Given its relatively close distance and high fluence, this source represents an ideal candidate for targeted follow-up observations. We emphasize that no afterglow has been observed from its earlier burst, and our calculations are intended to guide expectations and strategies for future observational campaigns.

3.2. Radio Afterglow

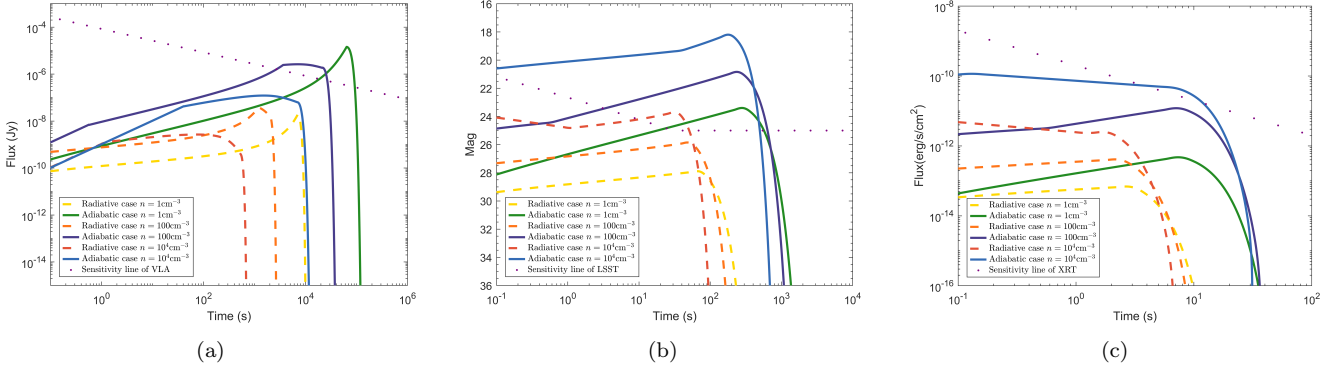


Figure 1. Multi-wavelength afterglow light curves of FRB 20171020A in different uniform media. The radio (1 GHz), optical (R-band), and X-ray (1 keV) light curves are shown for both radiative ($\epsilon = 1$, dashed lines) and adiabatic ($\epsilon = 0$, solid lines) cases. The detection limits of VLA (radio), LSST (optical), and Swift/XRT (X-ray) are indicated by purple dotted lines. Among them, (a), (b), (c) respectively represent the light variation curves under radio, optical and X-ray conditions.

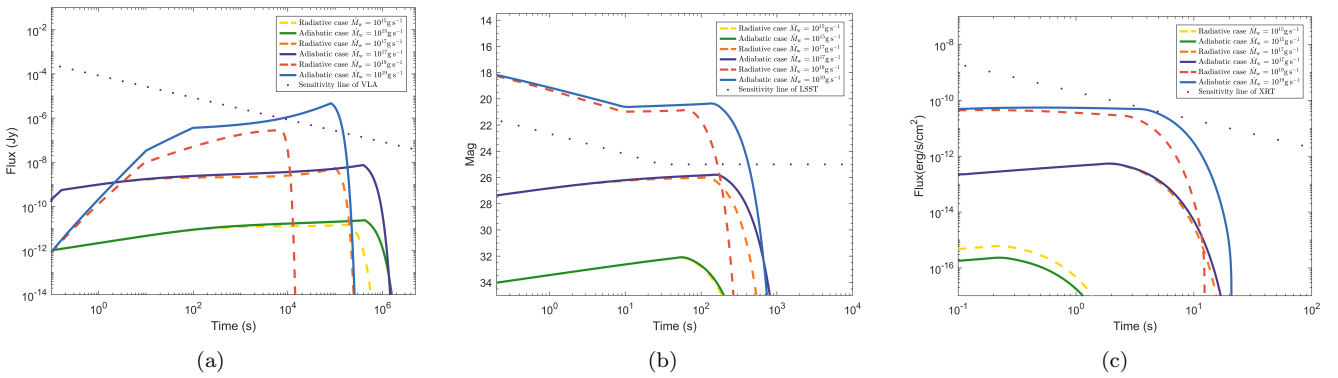


Figure 2. Same as Figure ??, but for a wind-like environment. The afterglow is generally brighter and longer-lasting than the uniform medium case, with the radio and optical signals exceeding detection limits in the adiabatic case. However, the X-ray afterglow remains undetectable with current instruments. Among them, (a), (b), (c) respectively represent the light variation curves under radio, optical and X-ray conditions.

Figures ??a and 2a display the radio afterglow light curves at 1 GHz in the uniform and wind-like environments, respectively. The evolution of the radio afterglow shows distinct characteristics in these two cases. In a uniform medium, Figure ??a shows the radio afterglow at 1 GHz. The peak flux densities for different density values are 1.59×10^{-9} Jy ($n = 10^4 \text{ cm}^{-3}$, red), 8.60×10^{-9} Jy ($n = 10^2 \text{ cm}^{-3}$, orange), and 1.84×10^{-8} Jy ($n = 1 \text{ cm}^{-3}$, yellow) in the radiative case, and 2.67×10^{-9} Jy ($n = 10^4 \text{ cm}^{-3}$, blue), 2.47×10^{-6} Jy ($n = 10^2 \text{ cm}^{-3}$, purple) and 1.39×10^{-5} Jy ($n = 1 \text{ cm}^{-3}$, green) in the adiabatic case. However, these flux levels mostly remain below the detection sensitivity of VLA, implying that radio follow-up in this scenario would be challenging. In a wind-like environment (Figure 2a), the radio afterglow is significantly brighter due to the denser medium. The peak flux increases to 2.34×10^{-11} Jy ($\dot{M}_w = 10^{15} \text{ gs}^{-1}$, yellow), 5.30×10^{-9} Jy ($\dot{M}_w = 10^{17} \text{ gs}^{-1}$, orange) and 2.70×10^{-7} Jy ($\dot{M}_w = 10^{19} \text{ gs}^{-1}$, red) in the radiative case. Importantly, the radio flux for the adiabatic case exceeds the VLA sensitivity, suggesting that a wind environment provides a better chance for radio afterglow detection. These results indicate that the detectability of the radio afterglow strongly depends on the external medium density. If FRB 20171020A originated in a wind-like environment, radio observations at the μJy level with facilities like the VLA or SKA are capable of detecting such afterglows.

adiabatic case, and 1.45×10^{-11} Jy ($\dot{M}_w = 10^{15} \text{ gs}^{-1}$, yellow), 5.30×10^{-9} Jy ($\dot{M}_w = 10^{17} \text{ gs}^{-1}$, orange) and 2.70×10^{-7} Jy ($\dot{M}_w = 10^{19} \text{ gs}^{-1}$, red) in the radiative case. Importantly, the radio flux for the adiabatic case exceeds the VLA sensitivity, suggesting that a wind environment provides a better chance for radio afterglow detection. These results indicate that the detectability of the radio afterglow strongly depends on the external medium density. If FRB 20171020A originated in a wind-like environment, radio observations at the μJy level with facilities like the VLA or SKA are capable of detecting such afterglows.

3.3. Optical Afterglow

Figures ??b and 2b show the optical afterglow in the R-band, compared to the LSST sensitivity limit. In a uniform medium (Figure ??b), the peak magnitudes are 27.9 ($n = 1 \text{ cm}^{-3}$, yellow), 25.8 ($n = 10^2 \text{ cm}^{-3}$, orange) and 23.6 ($n = 10^4 \text{ cm}^{-3}$, red) in the radiative case, and

23.4 ($n = 1 \text{ cm}^{-3}$, green), 20.8 ($n = 10^2 \text{ cm}^{-3}$, purple) and 18.1 ($n = 10^4 \text{ cm}^{-3}$, blue) in the adiabatic case. In a wind-like environment (Figure 2b), the peak magnitudes improve to 32.0 ($\dot{M}_w = 10^{15} \text{ g s}^{-1}$, yellow), 26.0 ($\dot{M}_w = 10^{17} \text{ g s}^{-1}$, orange) and 20.8 ($\dot{M}_w = 10^{19} \text{ g s}^{-1}$, red) in the radiative case. and 32.0 ($\dot{M}_w = 10^{15} \text{ g s}^{-1}$, green), 25.7 ($\dot{M}_w = 10^{17} \text{ g s}^{-1}$, purple) and 20.3 ($\dot{M}_w = 10^{19} \text{ g s}^{-1}$, blue) in the adiabatic case. These results suggest that LSST has an excellent chance of detecting the optical afterglow, but only if observations are conducted within a few hundred seconds post-burst. Rapid optical follow-up is crucial to capture the optical afterglow.

3.4. X-Ray Afterglow

Figures ??c and 2c show the X-ray afterglow at 1 keV, compared to the Swift/XRT sensitivity. In a uniform medium (Figure ??c), the X-ray afterglow is too faint to be detected. In a wind-like environment (Figure 2c), the X-ray flux is slightly higher but still remains below the Swift/XRT sensitivity threshold, even for the most optimal scenario. These results indicate that current X-ray facilities are unlikely to detect the afterglow of FRB 20171020A. However, future wide-field X-ray telescopes may improve detection prospects.

3.5. Detectability Across Parameter Space

To more comprehensively explore the detectability of afterglows across a wide parameter space, we present contour plots of the peak R-band magnitude as a function of kinetic energy and environmental density simultaneously, for both a uniform medium and a wind-like environment. Given our results that the optical band typically offers the highest detectability, we focus on the optical afterglow to assess observational prospects.

In our modeling, we consider two limiting cases for the shock evolution: adiabatic and radiative. In the adiabatic case, radiative energy losses are negligible, and most of the shock-generated internal energy is retained in the outflow. This corresponds to a radiation efficiency close to 0. In contrast, the radiative case assumes that nearly all of the internal energy is promptly radiated away, i.e., with 100% efficiency. These two cases represent the optimistic (adiabatic) and conservative (radiative) limits for predicting afterglow brightness. By analyzing both scenarios, we can bracket the expected range of optical flux and provide a robust assessment of detectability under varying physical conditions.

Figure 3 displays the contours in the $E_K - n$ plane for a uniform-density environment, where E_K ranges from 10^{40} to 10^{43} erg and the number density spans $1\text{--}10^4 \text{ cm}^{-3}$. The results show that the detectability of the optical afterglow varies significantly between the adiabatic and radiative regimes. Notably, in the adiabatic

case, detectable afterglows are possible for kinetic energies $> 10^{41}$ erg, while in the radiative case, the threshold for detection shifts to higher energies $> 10^{43}$ erg due to enhanced energy losses. Figure 4 shows similar contours in the $E_K - \dot{M}_w$ plane for a wind-like environment. As in Figure 3, the black dashed lines indicate the detection threshold of the LSST in the optical band. The contours reveal that only when the circum-burst environment is sufficiently dense (i.e., large \dot{M}_w) can a bright enough optical afterglow be produced to exceed the LSST detection limit.

These results suggest that the detectability of the afterglow from FRB 20171020A depends sensitively on both the energetics of the outflow and the density of the surrounding medium. In particular, detectable optical afterglows are expected only for events with kinetic energy $\gtrsim 10^{43}$ erg and dense local environments.

4. CONCLUSIONS AND DISCUSSIONS

We have investigated the possible multi-wavelength afterglow of FRB 20171020A, one of the closest and brightest extragalactic FRBs, using the thermal synchrotron emission model in a highly magnetized shock scenario. By considering two different external environments—a uniform medium and a stellar wind environment—we examined the afterglow evolution in radio, optical, and X-ray bands and assessed its detectability with current and future observational facilities.

Our results indicate that the optical afterglow is the most promising for detection, as it reaches a brightness significantly exceeding the LSST detection threshold. In both environmental scenarios, the optical afterglow is well above LSST's sensitivity, making it a strong candidate for follow-up observations. However, due to its rapid fading, it requires early observations within a few hundred seconds post-burst to maximize the likelihood of detection. This highlights the importance of rapid-response optical surveys in identifying FRB afterglows.

The radio afterglow, on the other hand, is much less certain. Only in the most favorable conditions, such as in a dense stellar wind environment, does the predicted radio flux exceed the VLA sensitivity threshold. Even in this case, detection remains challenging, and deep radio follow-up is required. In a uniform medium, the radio flux remains too low for current radio telescopes to detect. Therefore, while radio observations remain an important tool for constraining the FRB environment, their success depends strongly on the external medium properties.

The X-ray afterglow is expected to be too faint for detection with Neil Gehrels Swift/XRT, regardless of the environment. This suggests that current X-ray facilities

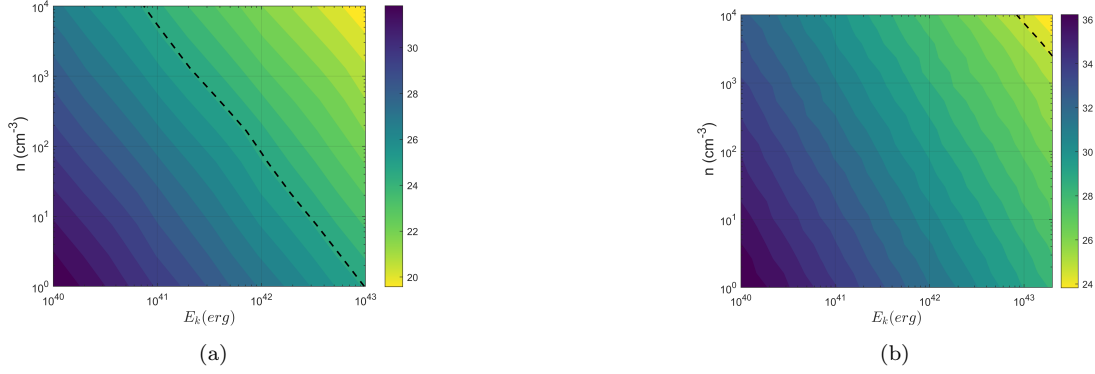


Figure 3. Contour of optical peak flux in the $E_K - n$ plane in a uniform medium. Different colors correspond to different optical peak flux levels (magnitude in the R-band). The black dashed lines indicate the LSST observational upper limits. Panel (a) represents the adiabatic case, while Panel (b) corresponds to the radiative case.

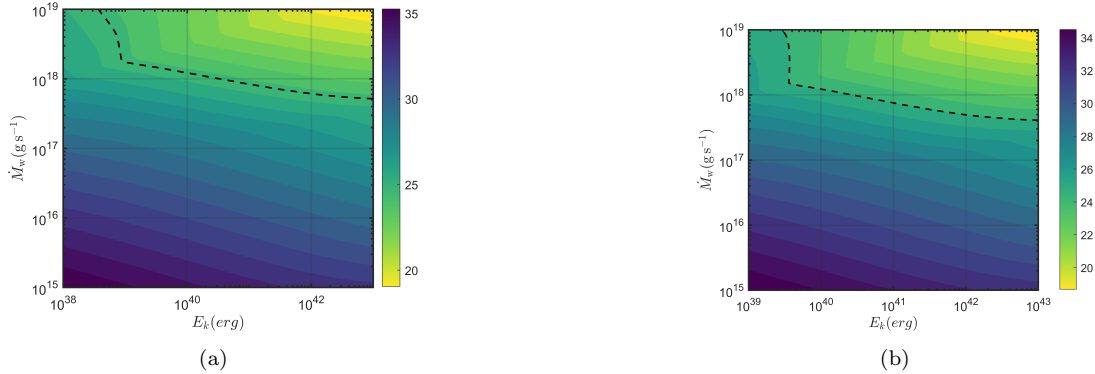


Figure 4. Contour of optical peak flux in the $E_K - \dot{M}_w$ plane for a wind-like environment. Different colors correspond to different optical peak flux levels (magnitude in the R-band). The black dashed lines indicate the LSST observational upper limits. Panel (a) represents the adiabatic case, while Panel (b) corresponds to the radiative case.

are unlikely to observe the high-energy counterpart of FRB 20171020A. However, future wide-field sensitive X-ray observatories may improve detection prospects.

Overall, our results demonstrate that the circum-burst environment plays a crucial role in shaping the afterglow properties. If FRB 20171020A is surrounded by a dense stellar wind, its afterglow is brighter and longer-lasting, improving the chances of detection. If it is instead propagating through a uniform medium, its afterglow is significantly weaker, making detection more difficult, especially in the radio band.

Given these findings, the best strategy for detecting FRB afterglows involves rapid optical follow-up with observational facilities like LSST, which offers the highest probability of success. Deep radio follow-up with VLA or SKA is still valuable but will likely only yield detections in favorable environmental conditions. Meanwhile, future X-ray surveys may help place additional constraints on FRB afterglow properties. As FRB discoveries continue to grow, nearby and bright events like

FRB 20171020A provide an excellent opportunity to test theoretical models and refine our understanding of FRB progenitors, their energy release mechanisms, and their connection to magnetars. Multi-wavelength follow-up of similar FRBs will be crucial for revealing the true nature of these mysterious radio transients.

Furthermore, it is natural to ask how frequently such nearby, energetic FRBs—capable of producing detectable afterglows—might occur and be observed in practice. Although the focus of this work is on FRB 20171020A and the possible multi-wavelength afterglow that may accompany its future bright bursts, we believe that discussing the general occurrence rate and detectability of nearby FRBs similar to FRB 20171020A is interesting. Such analysis also provides broader context and motivates the search for other nearby FRBs with similar observational potential.

From our model calculations, which explore a broad parameter space including variations in ambient density and dynamics, we find that afterglows become poten-

tially detectable only when the kinetic energy of the ejector exceeds $\sim 10^{43}$ erg. This threshold holds across various plausible environments (e.g., uniform or wind-like media) and dynamics. Given that typical FRB radiation efficiencies have been adopted to be $\sim 10^{-5}$ in this paper, we infer $E_{\text{FRB}} > 10^{38}$ erg as a practical threshold to identify nearby FRBs whose afterglows are realistically detectable.

Based on current estimates of the volumetric rate of FRBs with $E_{\text{FRB}} > 10^{38}$ erg, the occurrence rate is approximately $\sim 10^5 \text{ Gpc}^{-3} \text{ yr}^{-1}$ (Shin et al. 2023). Integrating over a volume up to 100 Mpc yields an all-sky rate of about 100 such nearby events per year. Considering that CHIME has a field of view covering approximately 0.3% of the sky, we estimate that it may detect ~ 0.3 nearby FRBs per year with sufficient energy to produce detectable afterglows. This low but non-negligible rate underscores the importance of rapid, multi-wavelength follow-up for exceptionally bright and nearby FRBs such as FRB 20171020A, and reinforces the need to identify and monitor nearby high-energy FRBs as prime candidates for afterglow searches.

Although this rate is low, it is not prohibitive. The greater challenge arises from the short lived nature of the predicted optical afterglow, which typically peaks and fades within ~ 100 s of the FRB event demanding extremely prompt follow-up observations. Assuming a typical 10% duty cycle for a single optical telescope, the probability of catching such an event is correspondingly small, implying that it could take approximately

30 years of continuous operation to detect a single afterglow

It is important to emphasize that our estimate represents a conservative lower bound. The assumed parameters—such as the minimum energy threshold and ambient environments—were chosen to reflect the most restrictive conditions under which the optical afterglow could still be marginally detectable. The actual detection probability may be substantially higher under more favorable (but still realistic) physical conditions. However, a reliable quantification of this would require a detailed Monte Carlo simulation across a high-dimensional parameter space, which lies beyond the scope of this work. This clearly illustrates the practical difficulty of detecting these rare but valuable transients, even for bright and nearby sources like FRB 20171020A.

Despite these challenges, several practical strategies could significantly improve the likelihood of detecting such afterglows. These include the deployment of robotic optical telescopes at geographically distributed sites to increase temporal and spatial coverage; the implementation of low-latency FRB detection pipelines capable of rapid DM-based distance estimation and event prioritization; and expanding the field of view and sensitivity of current and next-generation radio facilities to better capture rare nearby events in real time.

ACKNOWLEDGMENTS

This work is supported by the National Natural Science Foundation of China (grant No. 12203013) and the Guangxi Science Foundation (grant Nos. AD22035171 and 2023GXNSFBA026030).

REFERENCES

Arcus, W. R., James, C., Ekers, R., et al. 2025, PASA, 42, e003, doi: [10.1017/pasa.2024.114](https://doi.org/10.1017/pasa.2024.114)

Beloborodov, A. M. 2020, ApJ, 896, 142, doi: [10.3847/1538-4357/ab83eb](https://doi.org/10.3847/1538-4357/ab83eb)

Blandford, R. D., & McKee, C. F. 1976, Physics of Fluids, 19, 1130, doi: [10.1063/1.861619](https://doi.org/10.1063/1.861619)

Bochenek, C. D., Ravi, V., Belov, K. V., et al. 2020, Nature, 587, 59, doi: [10.1038/s41586-020-2872-x](https://doi.org/10.1038/s41586-020-2872-x)

CHIME/FRB Collaboration, Amiri, M., Bandura, K., et al. 2019, Nature, 566, 235, doi: [10.1038/s41586-018-0864-x](https://doi.org/10.1038/s41586-018-0864-x)

CHIME/FRB Collaboration, Andersen, B. C., Bandura, K. M., et al. 2020, Nature, 587, 54, doi: [10.1038/s41586-020-2863-y](https://doi.org/10.1038/s41586-020-2863-y)

CHIME/FRB Collaboration, Amiri, M., Andersen, B. C., et al. 2021, ApJS, 257, 59, doi: [10.3847/1538-4365/ac33ab](https://doi.org/10.3847/1538-4365/ac33ab)

Chime/FRB Collaboration, Andersen, B. C., Bandura, K., et al. 2023, ApJ, 947, 83, doi: [10.3847/1538-4357/acc6c1](https://doi.org/10.3847/1538-4357/acc6c1)

Cooper, A. J., Rowlinson, A., Wijers, R. A. M. J., et al. 2022, MNRAS, 517, 5483, doi: [10.1093/mnras/stac2951](https://doi.org/10.1093/mnras/stac2951)

Du, M., Yi, S.-X., Deng, C.-M., & Wang, P. 2023, Research in Astronomy and Astrophysics, 23, 115010, doi: [10.1088/1674-4527/acee53](https://doi.org/10.1088/1674-4527/acee53)

Feng, Y., Li, D., Yang, Y.-P., et al. 2022, Science, 375, 1266, doi: [10.1126/science.abl7759](https://doi.org/10.1126/science.abl7759)

Gao, H., Lei, W.-H., Zou, Y.-C., Wu, X.-F., & Zhang, B. 2013, New Astronomy Reviews, 57, 141, doi: <https://doi.org/10.1016/j.newar.2013.10.001>

Huang, Y. F., Dai, Z. G., & Lu, T. 1999, Monthly Notices of the Royal Astronomical Society, 309, 513, doi: [10.1046/j.1365-8711.1999.02887.x](https://doi.org/10.1046/j.1365-8711.1999.02887.x)

Kirsten, F., Marcote, B., Nimmo, K., et al. 2022, *Nature*, 602, 585, doi: [10.1038/s41586-021-04354-w](https://doi.org/10.1038/s41586-021-04354-w)

Kumar, P., Shannon, R. M., Osłowski, S., et al. 2019, *ApJL*, 887, L30, doi: [10.3847/2041-8213/ab5b08](https://doi.org/10.3847/2041-8213/ab5b08)

Lee-Waddell, K., James, C. W., Ryder, S. D., et al. 2023, *PASA*, 40, e029, doi: [10.1017/pasa.2023.27](https://doi.org/10.1017/pasa.2023.27)

Li, D., Wang, P., Zhu, W. W., et al. 2021, *Nature*, 598, 267, doi: [10.1038/s41586-021-03878-5](https://doi.org/10.1038/s41586-021-03878-5)

Lin, L., Zhang, C. F., Wang, P., et al. 2020, *Nature*, 587, 63, doi: [10.1038/s41586-020-2839-y](https://doi.org/10.1038/s41586-020-2839-y)

Lorimer, D. R., Bailes, M., McLaughlin, M. A., Narkevic, D. J., & Crawford, F. 2007, *Science*, 318, 777, doi: [10.1126/science.1147532](https://doi.org/10.1126/science.1147532)

Lorimer, D. R., McLaughlin, M. A., & Bailes, M. 2024, *Ap&SS*, 369, 59, doi: [10.1007/s10509-024-04322-6](https://doi.org/10.1007/s10509-024-04322-6)

Mahony, E. K., Ekers, R. D., Macquart, J.-P., et al. 2018, *ApJL*, 867, L10, doi: [10.3847/2041-8213/aae7cb](https://doi.org/10.3847/2041-8213/aae7cb)

Margalit, B., Beniamini, P., Sridhar, N., & Metzger, B. D. 2020, *ApJL*, 899, L27, doi: [10.3847/2041-8213/abac57](https://doi.org/10.3847/2041-8213/abac57)

Metzger, B. D., Margalit, B., & Sironi, L. 2019, *MNRAS*, 485, 4091, doi: [10.1093/mnras/stz700](https://doi.org/10.1093/mnras/stz700)

Moretti, A., Piotto, G., Arcidiacono, C., et al. 2008, *Astronomy and Astrophysics*, 493, 539. <https://www.aanda.org/articles/aa/abs/2009/02/aa10718-08/aa10718-08.html>

Nicastro, L., Guidorzi, C., Palazzi, E., et al. 2021, *Universe*, 7, 76, doi: [10.3390/universe7030076](https://doi.org/10.3390/universe7030076)

Nimmo, K., Hessels, J. W. T., Keimpema, A., et al. 2021, *Nature Astronomy*, 5, 594, doi: [10.1038/s41550-021-01321-3](https://doi.org/10.1038/s41550-021-01321-3)

Platts, E., Weltman, A., Walters, A., et al. 2020, *Physics Reports*, 821, 1, doi: [10.1016/j.physrep.2019.06.003](https://doi.org/10.1016/j.physrep.2019.06.003)

Pleunis, Z., Good, D. C., Kaspi, V. M., et al. 2021, *ApJ*, 923, 1, doi: [10.3847/1538-4357/ac33ac](https://doi.org/10.3847/1538-4357/ac33ac)

Sari, R., Piran, T., & Narayan, R. 1998, *The Astrophysical Journal*, 497, L17, doi: [10.1086/311269](https://doi.org/10.1086/311269)

Shin, K., Masui, K. W., Bhardwaj, M., et al. 2023, *ApJ*, 944, 105, doi: [10.3847/1538-4357/acaf06](https://doi.org/10.3847/1538-4357/acaf06)

Sironi, L., & Spitkovsky, A. 2009, *ApJ*, 698, 1523, doi: [10.1088/0004-637X/698/2/1523](https://doi.org/10.1088/0004-637X/698/2/1523)

Sokolowski, M., Bhat, N. D. R., Macquart, J. P., et al. 2018, *ApJL*, 867, L12, doi: [10.3847/2041-8213/aae58d](https://doi.org/10.3847/2041-8213/aae58d)

Thornton, D., Stappers, B., Bailes, M., et al. 2013, *Science*, 341, 53, doi: [10.1126/science.1236789](https://doi.org/10.1126/science.1236789)

Wu, X. F., Dai, Z. G., Huang, Y. F., & Lu, T. 2003, *MNRAS*, 342, 1131, doi: [10.1046/j.1365-8711.2003.06602.x](https://doi.org/10.1046/j.1365-8711.2003.06602.x)

Xiao, D., Wang, F., & Dai, Z. 2021, *Science China Physics, Mechanics, and Astronomy*, 64, 249501, doi: [10.1007/s11433-020-1661-7](https://doi.org/10.1007/s11433-020-1661-7)

Xu, H., Niu, J. R., Chen, P., et al. 2022, *Nature*, 609, 685, doi: [10.1038/s41586-022-05071-8](https://doi.org/10.1038/s41586-022-05071-8)

Yi, S.-X., Gao, H., & Zhang, B. 2014, *ApJL*, 792, L21, doi: [10.1088/2041-8205/792/1/L21](https://doi.org/10.1088/2041-8205/792/1/L21)

Zhang, B. 2020, *Nature*, 587, 45, doi: [10.1038/s41586-020-2828-1](https://doi.org/10.1038/s41586-020-2828-1)

Zhang, B. 2023, *Reviews of Modern Physics*, 95, 035005, doi: [10.1103/RevModPhys.95.035005](https://doi.org/10.1103/RevModPhys.95.035005)